Microtomography on polypropylene foam under dynamic loading: 3D analysis of bead morphology evolution

Philippe Viot [a,*], Erwan Plougonven [b], Dominique Bernard [b]

[a] LAMEFIP, ENSAM de Bordeaux, Esplanade des Arts et Métiers, 33405 Talence Cedex, France
[b] Institut de Chimie de la Matière Condensée de Bordeaux ICMCB, CNRS/Université Bordeaux I, 87 Avenue Dr. A. Schweitzer, 33608 Pessac Cedex, France

Received 14 May 2007; received in revised form 22 November 2007; accepted 26 November 2007

Abstract

A dynamic crash loading experiment is performed on polypropylene foam which is used in composite sandwich structures for safety applications. Several interrupted shocks are conducted, in between which, microtomographic acquisitions are made showing the change of the sample during its compression. These data can help construct and validate predictive models, although, because this material is multi-scale (constitutive beads at the mesoscopic scale are made of microscopic closed cells), image processing is required to extract useful quantitative measurements. Such processing is described here, so as to determine a representative volume for each bead of the sample, to associate values such as bead density to each bead and to each stage of the compression. This can help build a predictive model at the mesoscopic scale.

Keywords: A. Foam; B. Impact bahaviour; C. Computational modelling; Microtomography

1. Introduction

Composite multi-layers or sandwiches are becoming widely used in many industrial sectors for producing structural parts. Compiling an exhaustive list of all types of applications is difficult, but if we consider the transport sector, we find composite sandwiches for the aeronautic industry in key parts (wing leading edge, rudders). In the railroad industry, these structures are often used for wagon decor panels. As for the automotive and motorcycle industries, they are used in passive safety gear (bumpers or helmets). In all these applications, the intrinsic properties of light weight and rigidity are used. These sandwiches, composed of a core of cellular material and two composite skins, are light (since their constituents are of low density), rigid in traction and compression (the composite materials have good mechanical properties) but also in bending since the foam core thickens the structure (and thus increases its quadratic moment while limiting its weight) and supports high bending moments. These properties are particularly interesting for producing functional structures that must sustain high stresses under normal conditions. During severe or extreme loadings (crashes or accidents), these structures must deform plasticly and absorb the impact energy to protect either the rest of the structure or the passengers. In the case of a plane wing that can collide with a bird, the leading edge should be able to absorb the energy of the impact and lessen damage to the other structural elements. In a train accident, the composite decor panels must deform themselves if a passenger is thrown onto the structure. Finally, a car is the first passive safety element that protects the vehicle passenger or pedestrian involved in the accident. It is thus imperative to control the response of composite sandwiches to high strain rates. Characterization of the behavior of the composite material and core cellular material under dynamic loadings is essential before considering numerical modeling of the real structure. The study we are particularly concerned with is the description of the cellular material behavior during dynamic loading.

* Corresponding author. Tel.: +33 5 56 84 53 62; fax: +33 5 56 84 53 66.
E-mail address: philippe.viot@lamef.bordeaux.ensam.fr (P. Viot).

doi:10.1016/j.compositesa.2007.11.014

Many studies have been carried out at the macroscopic scale to characterize experimentally the behavior of this type of material under dynamic stresses. Di landro et al. [1] studied experimentally the behavior of polystyrene foams. Static and dynamic compression tests (with classical testing machine and drop tower) were done to identify the parameters of a constitutive model as function of strain rate and temperature. A complementary observation of the microstructure has been done to reveal the deformation of the beads and the buckling of their walls. The compressive behavior of polystyrene foam was also experimentally investigated by Song et al. [2] at strain rates from 0.001 to 950 s^{-1} by using testing machine and Hopkinson bars. Avalle et al. [3] have done equivalent studies on polypropylene, polystyrene and polyurethane foams in quasi static and dynamic loading. From the results, he deduced absorbed energy – stress diagrams allowing the definition of the most efficient foam (nature and density) in function of the applications. Zhang et al. [3,4] have completed the database on these cellular materials by carrying out uniaxial and hydrostatic loadings and simple shear tests for different strain rates. All these experiments show that the behavior of cellular material generally includes three steps in compression: an elastic response, a plastic regime with an important deformation of the material and quasi-constant stress, and finally a densification. It is the stress plateau of the plastic phase that is of interest for passive security applications since the material can absorb a significant fraction of the impact kinetic energy. From these experimental results, empirical laws were proposed to describe more or less accurately the relation between stress and strain according to different parameters such as density and strain rate (eventually the temperature). For instance, Gibson and Ashby [6] and Zhang et al. [5,7] studied the macroscopic behavior of polymeric and metallic foams under multi-axial loading and for different strain rate conditions. From these studies, yield surfaces were proposed for analysing the behavior of foams by different approaches. On the one hand, Gibson and Ashby proposed constitutive equations for polyurethane, polyethylene and aluminium foams (closed or open cells) based on the analysis of the macroscopic mechanical response of a foam ideal structure. On the other hand, from the macroscopic behavior identified experimentally, Zhang developed also a rate dependent constitutive equation without taking into account any strain localization. Some of these models have been already implemented in Finite Element codes such as ABAQUS [8] or LS DYNA [9]. In any case, these models consider the macroscopic response of a homogenized material but do not take into account the localizations of the observed strains and thus their heterogeneity.

These laws, used in industry and numerically adjusted on the global stress curves, can be used to represent the behavior of a large variety of cellular materials such as polymeric or aluminium foams. It is well known that for the former, the predominant phenomenon in its damage is the wall buckling of the constitutive cells whereas wall fractures can be observed in the latter. It is therefore essential to propose macroscopic behavior models which take into account the physical phenomena observed at all scales (macroscopic scale, bead scale in the case of expanded polymeric foams and cell scale) of the cellular material structure.

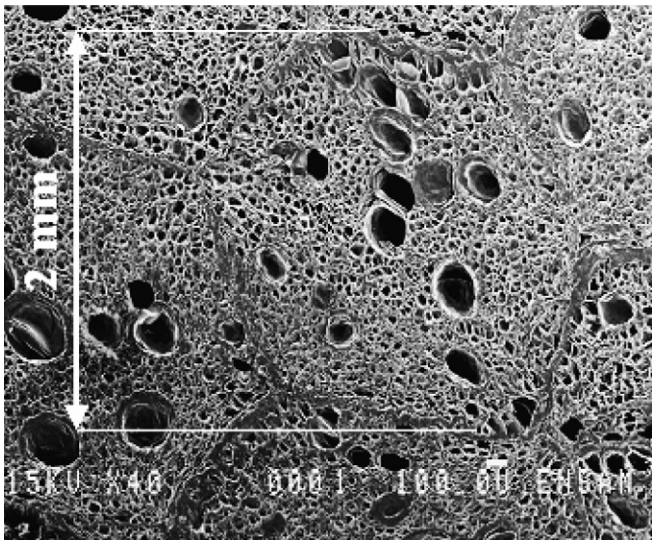

Fig. 1a. Micrograph of polypropylene foam showing the bead structure.

This study is part of a work which aims to propose a behavior multi-scale model based on the physical phenomena observed on expanded polymeric foam during dynamic loading. The structure of the considered polypropylene foam is multi-scale: at the mesoscopic scale, as seen in Fig. 1a, the material consists of porous polypropylene beads agglomerated during manufacturing, beads that are composed of thousands of small closed cells, shown in Fig. 1b (microscopic scale). Behavior of this type of material under dynamic stress is thus foreseen by a multi-scale description. It is obviously necessary to identify the global

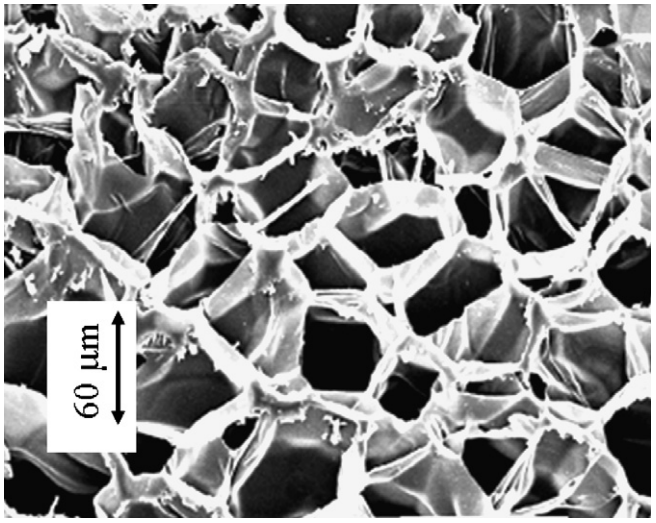

Fig. 1b. Micrograph of polypropylene foam showing the cell structure.

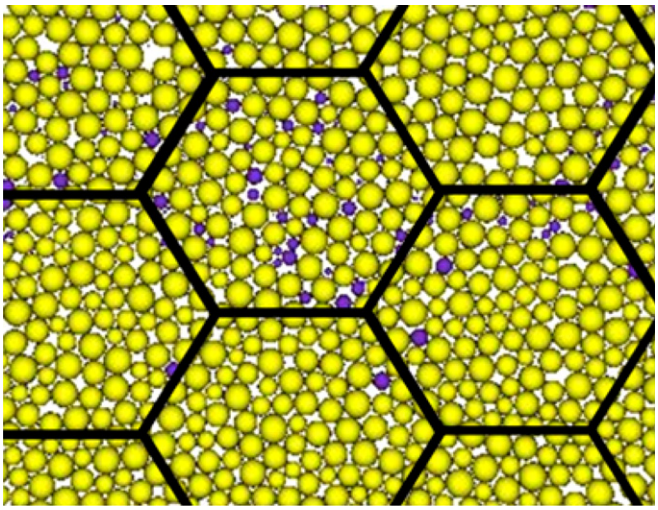

Fig. 1c. Multi-scale modeling scheme of foam.

response of materials at the macroscopic scale for various strain rates, but also to investigate the response of the foam structure at the mesoscopic (that of the bead) and microscopic scales (that of the basic cell). Observation of the deformation of the meso- and microscopic walls (bead and cell) will be one of the elements that will help to establish phenomenological laws at these scales.

The method proposed to reach the final objective of this work is to model the micro (cell scale) and mesostructure (bead scale) of the foam sample. The first step, presented in this paper, concerns the identification of a mesostructure of a polypropylene foam sample. The representativeness of the sample for the macroscopic material is less important than for the homogenisation method since the next step is the modeling of the real sample mesostructure (bead scale). The study of the microstructure (cell scale) is simultaneously in progress.

Homogenisation methods will afterwards be used to build a multi-scale model describing the foam response at the macroscopic scale. In this article are presented the observation, the comprehension and the characterization of the physical phenomena occurring in the multi-scale structure of the foam. This step is essential to reach the final objective of foam structure modeling. The following steps will be to represent the specific structure of the studied sample by a polyhedral mesh taking into account the two meso- and microscopic scales of the material (Fig. 1c) and to derive a macroscopic model fitting experimental results with numerical simulation ones.

2. Material and methodology

2.1. Polypropylene foam

A polypropylene foam is investigated in this paper. The plates of cellular material are obtained by moulding; the expanded plastic foam beads are injected into a plate mould (700 mm × 400 mm × 24 mm), where individual beads are fused together under steam heat and pressure. The average density of each plate intrinsically depends on the quantity of expanded beads injected into the mould. For this study, the density of the plate is 80 kg/m^3. The moulding process, particularly injector and vent positions, induces density heterogeneities. Horizontally, measurements on a large number of samples cut out from this plate show values as large as 92 kg/m^3. Vertically, i.e., through the thickness of the plate, density increases significantly near the surfaces (12%), whereas in the central region it is relatively uniform. Consequently, the samples were obtained by coring a cylinder perpendicularly to the plate and upper and lower parts were cut to reach the final dimensions (10 mm in diameter and height).

2.2. Methodology

The physical phenomena observed on polymeric foams during dynamic compression has already been studied under specific conditions [10]. After impact, the buckling of both cell and bead walls have been observed by SEM. A strong heterogeneity of the residual deformation can be seen. However, the main difficulty of these observations lies in the sample cutting.

Complementary measurements were taken during impact with the use of optical acquisition apparatus and image processing techniques (high-speed camera, optical fibre spotlights and Digital Image Correlation software). A strong heterogeneity of the strain field was shown, and strain localizations appear in layers perpendicular to the loading direction. The material damage progresses close to these zones during the stress plateau [10,11]. However these observations are only possible on the free faces of the sample, implying that this method cannot estimate the strain field inside the foam structure.

In light of these first results, microtomography was considered for observing the deformation inside the foam structure. Tomography is a non-invasive process of generating images of cross-sections from a series of transmission data acquired by illuminating the object from different directions [12]. In the case of X-ray tomography, for each direction of illumination, the process is similar to radiography: the acquired transmission data gives a map of the rays attenuation. Fig. 2 illustrates this: the centre object, consisting of an ellipse and a circle, is illuminated from two directions by a parallel beam, the acquired images are called projections, which are used to reconstruct cross-sections of the object. In reality, many more projections are needed for an accurate reconstruction using, for instance, filtered back-projection [12].

Microtomography has been already used to characterize foam microstructures for different applications. For instance, to optimize Processing of Aluminium [13] or polymeric foams [14], cell structures (size distribution, wall thickness, connectivity, etc.) were quantified after specific 3D image treatments. The reconstructed 3D images can be also used to compute effective physical properties of

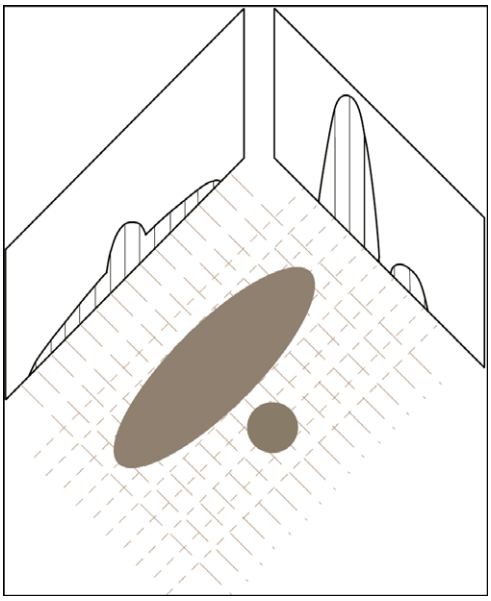

Fig. 2. Illustration of the principle of parallel beam X-ray tomography.

the foam like permeability diffusivity and macroscopic mechanical properties [15]. Taking advantage of the fact that this technique is non-destructive, the change of the microstructure of a given sample can be followed in 3D during a mechanical test. McDonald et al. [16] studied in situ the strain localization at the cell scale for an aluminium foam during quasi static compression.

Those studies demonstrate the relevance of microtomography to identify a foam structure without loading [13–15] or during a compression test [16]. In our case, there are two extra difficulties. First, the polymeric foam considered here has a multi-scale structure constituted of large beads and micro closed cells, making the segmentation more complex and requiring development of specific image analysis procedure. Second, the loading is dynamic (punch displacement speed 5 m s^{-1}) and the structure measurement cannot be done in situ. In consequence, identification of the foam deformation and damage propagation in 3D from microtomography measurements requires an original dynamic test methodology [17]. The adopted experimental approach consists in carrying out several interrupted impacts on a given sample using a drop tower, and acquiring a micro tomogram in between each impact. The sample (diameter and height of 10 mm) is scanned a first time before the first impact. During each compression, the deformation amplitude is limited to fixed values: 1 mm for the first impact and 2 mm for the following ones. Fig. 3 shows on the stress–strain curves the different states the sample was in when acquisitions were made. The sample is maintained compressed and replaced on the microtomography setup for another acquisition (points A, B, C, etc.). A second micro tomogram is recorded when the sample is completely unloaded (points A′,B′, C′, etc.). These operations (impact and 2 X-ray scans) are repeated until densification of the foam. The cellular material strain can then be evaluated

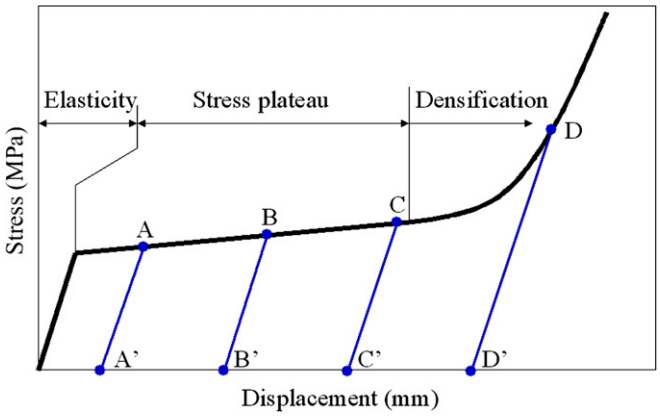

Fig. 3. Typical evolution of compression stress vs strain for a cellular material.

from the 3D reconstructions at each stage of the dynamic test.

Micro tomographic images presented in this paper have been obtained on the BM05 beam line at the European Synchrotron Radiation Facility (ESRF) in Grenoble (France), with beam energy of 16 keV. The acquired projections (1200 in our case) are 2028 × 2048 pixels radiographs, with a pixel corresponding to 4.91 μm.

The 3D reconstruction uses pre- and post-processing to reduce artefacts and noise, such as hot spots or ring artefacts.

From these measurements, a first analysis was done in 2D. The deformation of beads located in a vertical section of the foam was calculated for each step of the experiment [17] and bead density was estimated. This first study shows that there is not a strong correlation between the density of beads and their volume deformation, meaning that bead density is not the principal parameter influencing the deformation heterogeneity. However, the arrangement of beads, their shapes and the geometry of the mesostructure seem to have an influence on the strain field. This can be checked by 3D analysis of a larger number of beads of different density. Contrary to 2D study for which planar displacements are assumed, the volume strain is calculated directly from the change of bead volume and the bead displacement is determined from the location of its barycentre.

The main difficulty of a 3D analysis is to extract the bead walls from the multi-scale structure: Fig. 4 shows that it is difficult even interactively to accurately position the walls. This problem is minimised for other types of foams that have been more extensively studied, such as metallic foams. Typical digital image filters are not sufficient to extract these complex walls: noise reduction and threshold produce structures with unrealistic porous zones and traces of cells or bubbles with thick walls, as illustrated in Fig. 5, which cannot be used, neither to quantify bead volume changes, nor to generate a FE mesh of the foam morphology. To overcome this, a new approach for identifying the bead structure was developed. The method requires a perspicacious sequence of typical image processing operations

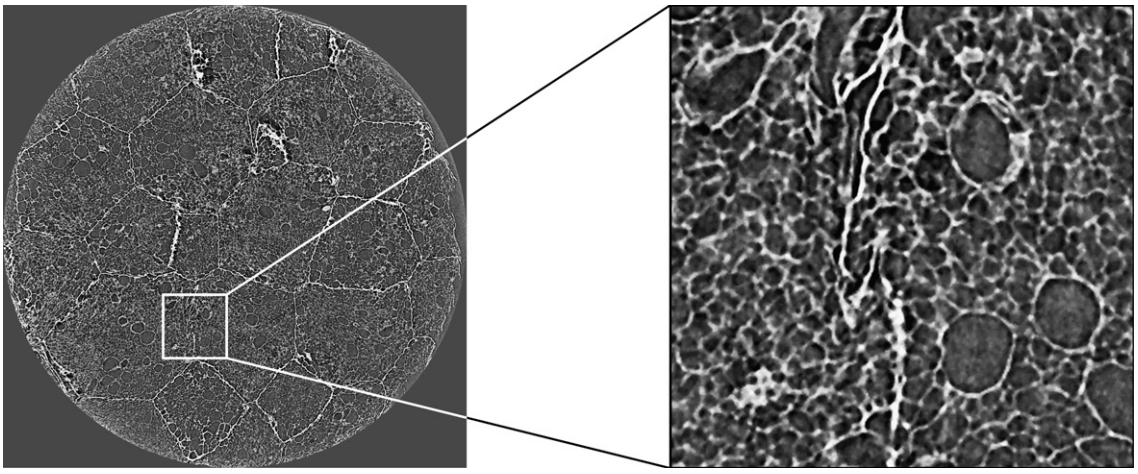

Fig. 4. An axial cross-section of a micro tomogram of the studied polypropylene foam. The left image is a view of the entire section, where the bead walls seem well -defined. The image on the right is a zoomed portion of the image, an example of why localizing these walls with precision is not possible.

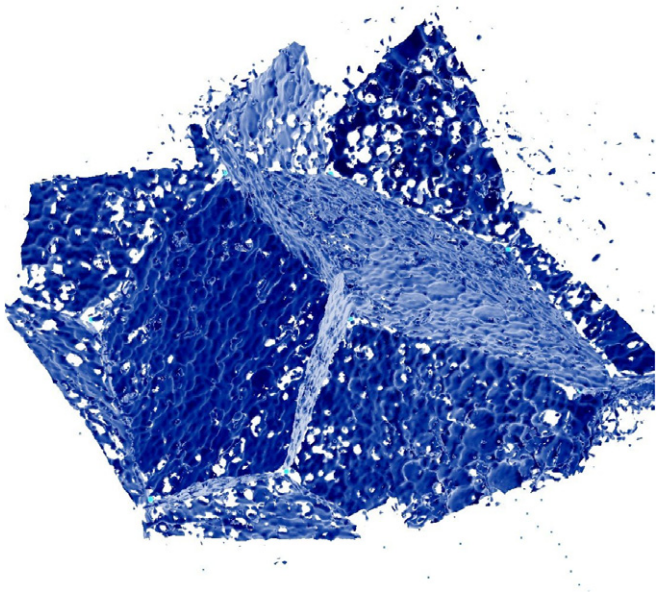

Fig. 5. 3D reconstruction of bead walls in using classical numerical filters.

to extract a more accurate representation of the bead structure that is useable for calculating bead strain.

This paper presents the image analysis that was implemented to identify distinct regions in the microtomograms for each bead that makes up the foam. The method was applied at several steps of the loading and the evolution of bead strain can be estimated and compared to bead density.

3. Image analysis methodology

The purpose of this work is to understand the behavior of polypropylene foam at the mesoscopic scale (scale of the beads), for which extracting pertinent data from the microtomographic images is required. To perform measurements on the beads, a representative volume in each one is determined. The final objective of this work is to follow the deformation of these Representative Bead Volumes (RBV) and to estimate the influence of bead density. This section describes the way these volumes are extracted.

The method consists of two steps: firstly, a series of filters applied on the reconstructed volumes gives approximate positions for the bead centres, and secondly each centre serves as starting point for a deformable surface algorithm, in which a triangulated surface placed inside a bead expands until coming in contact with bead walls. These surfaces are used to delimit representative bead volumes in the microtomograms.

3.1. Extracting approximate bead centres

Estimating bead centre positions requires a sequence of basic filtering operators to be applied on the reconstructed image. Fig. 6 summarises the filtering sequence, and Fig. 7 shows various intermediary results. First, the image is subsampled: each 4-pixel wide cube in the image is replaced by one pixel, dividing the size of the numerical volume by 64 (step a). This was done because of hardware limitations, but in no way affects the correctness of the method. The next operation partially removes phase contrast (due to X-ray diffraction at the interfaces between phases of the sample, an enhanced contrast appears around portions of bead and cell walls [18]) by removing darker areas: if a pixel p has an intensity i lower than the intensity i_0, equivalent to the attenuation of the air, then it is set to i_0 (step b). The reason for this is that at some point small features such as noise and microscopic cells need to be smoothed out, and if a gaussian filter is applied on the image containing phase constrast, i.e., light zones next to dark ones, a smoothing operator will level these areas to that of the rest of the image. A gaussian filter (step c) is then applied to remove noise and microscale features inside the beads. The next operator (step d), a gradient (the Sobel norm was used), highlights the bead edges.

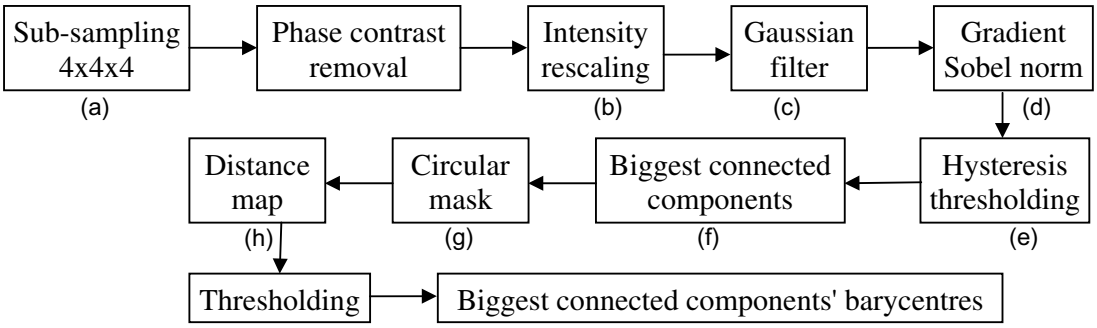

Fig. 6. Method applied to the reconstructed microtomograms to extract approximate grain centres. Some parameters (such as the threshold levels) need to be manually set. Illustrations at steps (a)–(h) are presented in Fig. 7.

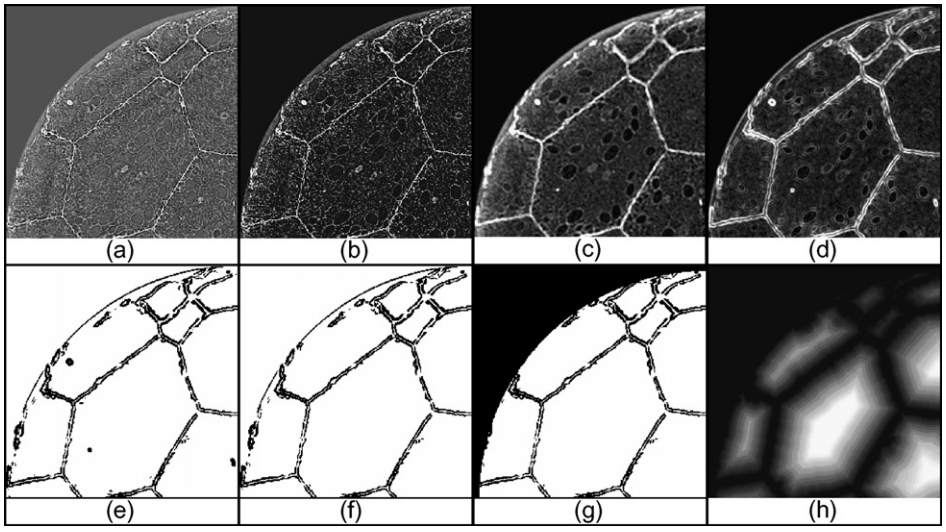

Fig. 7. Illustration of the method used to extract approximate positions of the grain centres. It consists of a series of simple arithmetic and morphological operators on the microtomograms (for visibility, figures (e)–(g) are inverted).

The next part consists of extracting *most* pixels from the bead walls, which is where the gradient is higher. Operations described here are based on notions of digital topology [19]. First a hysteresis thresholding is applied (i.e., the image is thresholded with a high and low value, giving two binarised images, respectively I_h and I_l, then a geodesic dilation is applied to I_h in I_l [20]), which makes for a better binarisation than a classical thresholding since the bead walls are connected (step e). The thresholds are chosen so as to extract enough of the bead walls to obtain a single connected component for these pixels, and as little as possible of the inside of the beads. The result does not contain all the pixels of the bead walls and contains a few noticeable cells around and inside the beads. The cells around the bead walls hardly affect the bead centre approximation, but the ones inside the cells should be removed, which is done by extracting the largest connected component (step f). Afterwards, to avoid the unreconstructed area of the image to influence the ensuing operations, a cylindrical mask is applied (step g): the resulting image has foreground pixels belonging either to the unreconstructed areas of the image or the bead wall borders.

The resulting image at step g is used to compute an euclidian distance map (i.e., the intensity of each pixel of the background is set to its distance from the foreground), in which pixels close to the bead centre are darker, and those in and around the bead walls are lighter (step h). The distance map is then binarised by a thresholding operator (with a threshold value high enough to disconnect all the beads, since portions of the bead walls were missing from the image used for the distance map). In the binarised image, smaller connected components that appear at junctions between beads due to artifacts from the previous operations are removed. Finally an image with as many connected components as there are beads in the sample is obtained. What is finally defined as bead centres is the barycentres of these connected components. Fig. 8 depicts this result: an isosurface of the distance map is drawn, with the isosurface value corresponding to the threshold used.

3.2. Deformable surfaces

Each bead centre serves as initial position for a deformable surface: a closed triangulated surface, initially having

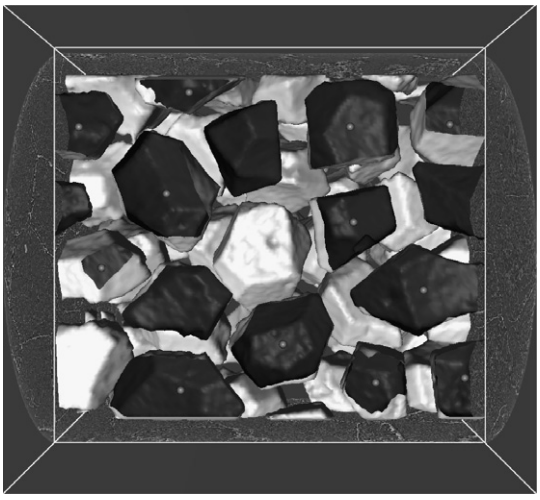

Fig. 8. Representation of the distance map threshold which allows locating bead centres. An isosurface of the distance map (Fig. 7h), with the threshold value used for finding the barycentres, is displayed. The dots inside the isosurfaces are the bead centres.

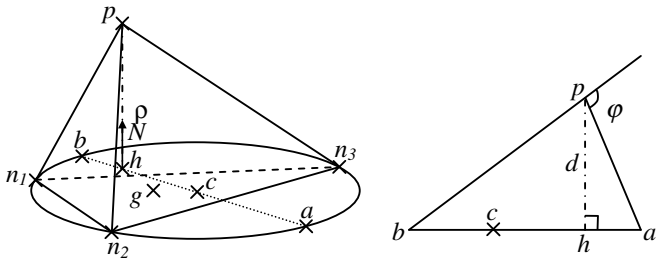

Fig. 9. Simplex angle and elevation of a vertex of the deformable mesh, used to regularise the mesh to obtain a smooth surface. p is the considered vertex, n_1, n_2 and n_3 are its neighbours, h is projection of p on the plane defined by the triangle $n_1n_2n_3$, c is the centre of the circle circumscribing $n_1n_2n_3$, a and b are the points of the circle aligned with (hc), and g is the triangle's centre of gravity. Finally, d is called the elevation and φ the simplex angle of p.

a spherical shape, is placed inside the bead and expands under given conditions such that it converges towards pixels of higher intensity, i.e., bead walls.

It might be suggested that the volumes delimited by the isosurfaces used to define the centres can be directly used to estimate bead strain. However, the volumes of the isosurfaces identified are not large enough to be considered representative of the bead (the set of isosurfaces only encompass about 35% of the sample volume). By using a deformable surface algorithm, larger portions of the bead interiors are determined (around 75%) which account for a better bead representativity.

To obtain an RBV, the implemented algorithm is based on the works of Delingette et al. [21,22]. The evolution of the surface, which is a 3-simple mesh (a mesh in which each vertex is contained in exactly 3 facets), is an explicit model, i.e. the evolution is calculated at each step t, and is made by subjecting each vertex p of the mesh to a second-order Newtonian law of motion $\sum_{m=d,i,v,r}\vec{F}_m = m\vec{a}$, where $\vec{F}_m$ represents several forces, classified as internal and external to the mesh, m a mass assigned to the vertex p and $\vec{a}$ its acceleration. The forces are defined as: a dilation force $\vec{F}_\mathrm{d} = k_\mathrm{d}\vec{N}$ expands the surface, an opposite intensity force $\vec{F}_\mathrm{i} = -k_\mathrm{i}\vec{N}$, which increases when the vertex is inside a high-intensity region of the image, contracts the surface, and a viscosity force $\vec{F}_\mathrm{v} = k_\mathrm{v}\vec{V}$ adds friction to the movement to avoid divergence. The constants k_x are manually set to optimize the convergence of the surface, the vectors $\vec{V}$ and $\vec{N}$ are respectively the speed of p and the normal of the plane defined by the three neighbours n_1, n_2 and n_3 of p (the neighbours are oriented so that the normal always points outwards). The internal force is a regularisation force $\vec{F}_\mathrm{r} = k_\mathrm{r}(\vec{g} + \tilde{d}\vec{N} - \vec{p})$ that smoothes the curvature of the surface. The curvature is based on the elevation d of the vertex, which is controlled by its simplex angle ϕ, as shown in Fig. 9. The value $\tilde{d}$ represents the elevation, above the centre of gravity of the triangle $n_1n_2n_3$, of a point that has a simplex angle $\tilde{\varphi} = \sin^{-1}\left(r\sum_{j\in[1;3]}\frac{\sin\varphi_j}{r_j}\right)$, where r is the radius of the circle circumscribing the triangle, and ϕ_j and r_j are respectively the simplex angle of n_j and radius of the circle circumscribing the neighbours of n_j. Convergence is achieved when, for each vertex, all forces are balanced and speed drops to zero.

An essential factor for this approach is the choice of the image that defines the force field $\vec{F}_i$. This image should contain higher intensity values near the areas where the deformable mesh is to converge. Although the initial image, the reconstructed microtomogram, appears to have suitable features for this process, the amount of noise, significant cell wall intensity and higher intensity near the sample periphery make it an inappropriate choice. The best results were obtained with a smoothed gradient, as in step d of Fig. 7. To avoid surfaces expanding outside of the sample bounding volume, a cylindrical mask was applied to this image, as in step g. Results of this algorithm (obtained, in less 60 s per bead, from the image of the sample before impact) are shown in Figs. 10a and 10b: each bead is represented by a surface, and compared to Fig. 8, these surfaces are more tightly packed. There is still however a notable interstitial volume in between the beads, which has no physical significance: in the material, foam beads are in contact with each other and no space exists between them (except in some regions neighbour to three or more beads). This is due both to areas where bead delimitations are not marked by strong intensity variations, and to cell walls which are as pronounced as bead walls (even to the naked eye it is sometimes unclear where bead walls are located, see Fig. 4). Nevertheless, the present task is not to completely encompass the bead volumes, but to obtain an RBV.

4. Results

This methodology is applied on the polypropylene foam sample and for each stage of dynamic loading. The first numerical process makes it possible to detect 87 bead

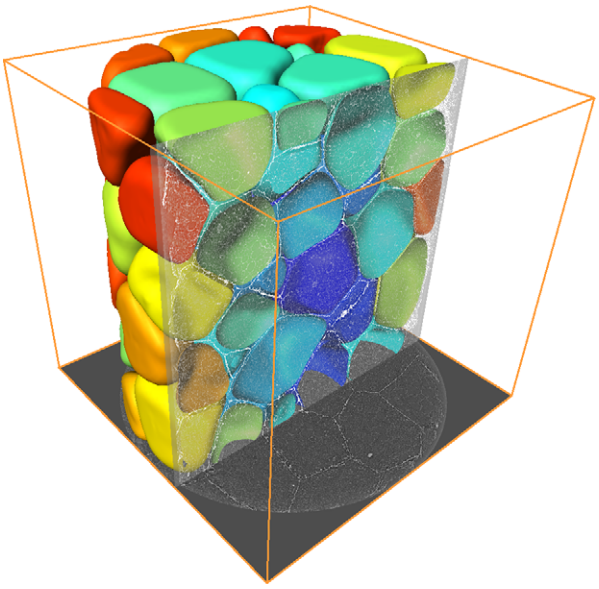

Fig. 10a. A view of the calculated surfaces that delimit the grains, with a colour map corresponding to the relative density of the beads. Beads at the periphery are noticeably denser.

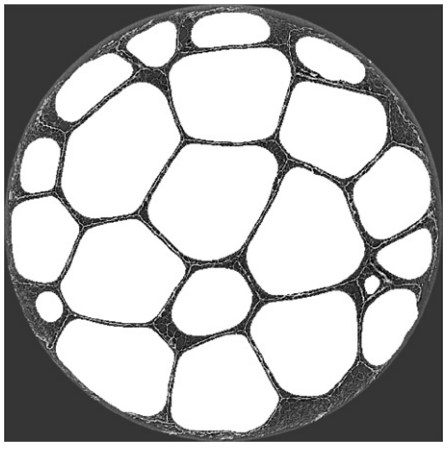

Fig. 10b. Section in the middle of the sample showing the interstitial volume between reconstructed beads (sections in white).

centres. From these points, the deformable surface algorithm was used to create 87 meshes corresponding to the representative volume of foam beads (Figs. 11 and 16a, b and c). This method was applied for all the acquired tomograms (points A, A′, B, B′..., Fig. 3). It is then possible to represent the sample as a set of surfaces and better visualise its deformation during the experiment: Fig. 11 shows this representation before impact and after the second impact (respectively left and right view). Each mesh can then be extracted and its deformation, which approximated that of the corresponding bead, studied separately; in many cases, the bead strain is more complex than the strain obtained under a simple homogeneous uniaxial compression. For instance, if we consider the bead marked as number 61 and shown in Fig. 12, visual analysis for the two first impacts reveals a inhomogeneous deformation; the lower portion of the mesh seems to become more compressed than the rest [23].

This qualitative observation can be completed by quantitative measurement in using the features of numerical algorithm. Firstly, for each bead, voxels contained in the RBV are counted: this gives a lower bound of the bead volumes. The objective of this procedure is to extract the internal part of the beads constituted only of porous material. The efficiency of this method can be estimated by the ratio K_v between the total volume of reconstructed beads and the one of the sample. For the CT-scans before loading and after the first and second impacts, this ratio K_v is close to 0.74. For the third and fourth impacts (where the macroscopic strain reaches 50% and 70%), this ratio is, respectively 0.64 and 0.51. It means that this algorithm is sufficiently precise to extract for further treatments more than half of the volume even for deformations as large as 70%.

Secondly, an average grey level can be calculated for each bead, by using the intensities of the pixels of the tomograms that are contained in its corresponding mesh. With common image processing software, the average grey level of each RBV was calculated. Theoretically, in particular neglecting the phase contrast effects, there is a linear relation between the grey level of a pixel and the density of the corresponding volume element. Indeed, the tomographic reconstruction produces a 3D mapping of μ, the linear attenuation coefficient of the material. The grey level image is obtained by applying the following affine transformation to this 3D mapping: the grey level assigned to the pixels having a value lower than μ_{min} is 0. for the pixels having a value larger than μ_{max} it is 255, and in between a linear interpolation is applied. The values of μ_{min} and μ_{max} are selected to optimize the dynamic of the grey level image. This is done by thresholding the cumulated histogram of the μ values.

Noting that

$$\begin{aligned} \mu_{air} &\ll \mu_{pp} \\ \rho_{air} &\ll \rho_{pp} \end{aligned} \tag{1}$$

the following relations can be obtained:

$$\begin{aligned} \mu &\cong (1-\phi)\mu_{pp} \\ \rho &\cong (1-\phi)\rho_{pp} \end{aligned} \tag{2}$$

where ρ is the density, ϕ the porosity, and subscripts 'air' and 'pp' refer, respectively to air and polypropylene.

Rewriting Eq. (2)

$$\begin{aligned} \phi_{i,j,\alpha} &= 1 - \frac{\mu_{i,j,\alpha}}{\mu_{pp}} \\ \rho_{i,0.\alpha} &= \frac{\mu_{i,0.\alpha}}{\mu_{pp}}\rho_{pp} \end{aligned} \tag{3}$$

where i is the bead number, j the compression stage (0 before loading, 1 after the first impact, point A in Fig. 3, and so forth) and α characterizes the loading state: $\alpha = c$ (compressed) or $\alpha = u$ (unloaded). The μ values are calculated

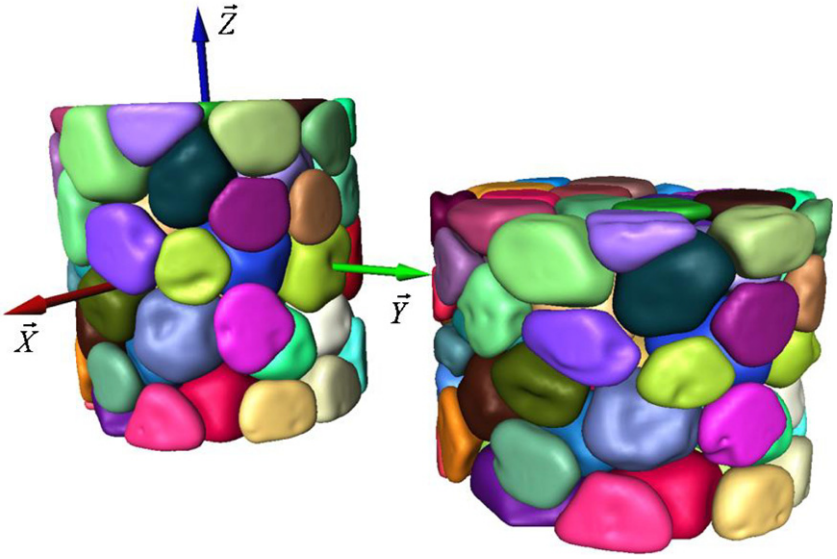

Fig. 11. Reconstruction of bead morphology: before compression (left picture) and after the second impact (right picture). Each bead is identified by its colour.

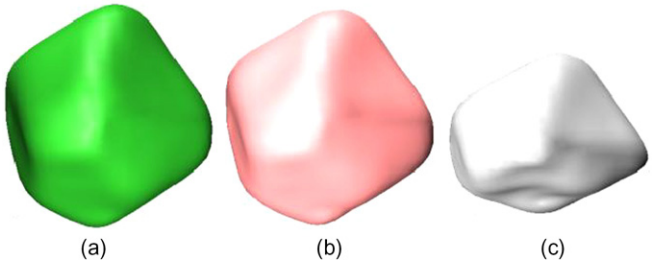

Fig. 12. Reconstruction of the morphology of bead 61: before compression (a), after the first impact (b) and after the second one (c).

from the grey level using the linear relation applicable between $\mu_{\min}$ and $\mu_{\max}$.

A volume variable can be chosen to estimate the deformation of each bead. If we consider the strain tensor $\bar{\bar{\varepsilon}}$, the trace of this tensor corresponds to the volume strain of the material $\varepsilon^{\text{vol}} = \text{tr}(\bar{\bar{\varepsilon}})$. The volume strain of a porous media can be calculated from its porosity. In our case, the volume strain of a bead i, due to the dynamic loading (step j), is obtained from the relation:

$$\varepsilon^{\text{vol}}_{i,j,\alpha} = 1 - \frac{\phi_{i,j,\alpha} - \phi_{i,0.\alpha}}{1 - \phi_{i,j,\alpha}} \tag{4}$$

It is then possible to retrieve the volume strain of each bead from the variation of its mean grey level in combining Eqs. (3) and (4):

$$\varepsilon^{\text{vol}}_{i,j,\alpha} = \frac{\mu_{i,0.\alpha} - \mu_{i,j,\alpha}}{\mu_{i,j,\alpha}} \tag{5}$$

4.1. Foam morphology

4.1.1. Bead size

For each bead, the number of voxels contained in the mesh multiplied by the corresponding volume $((4.91\ \mu\text{m})^3$ in this case) approximately measures the RBV. This first calculation gives an indication on the bead size variability before the loading. Initially, the mean volume of the RVBs is 6.7 mm^3, ranging from 0.8 mm^3 to 12.9 mm^3. The smallest RBVs correspond to the outer beads that have been cut during sample preparation. If we omit these incomplete beads, the mean volume rises to 9.7 mm^3, ranging from 6.2 mm^3 to 12.9 mm^3. Assuming that there is a good correlation between the computed RBV and the corresponding bead in terms of volume, we observe a strong heterogeneity in bead size for the sample before impact. Paragraph 4.2 analyses the effect of this heterogeneity on bead deformation.

4.1.2. Bead density

Theoretically, using Eq. (3) the average density of a bead can be obtained from the grey levels of all pixels contained in that bead. It can be approximated by using the pixels contained in the corresponding RBV. In practice, the average grey levels obtained for each bead varies only weakly, from 77 to 84. The measurement dynamics, calculated as the ratio of grey level variation (84–77) to the measurement range (256), does not exceed 3%. Those grey levels correspond to bead porosities ranging from 98% to 78% (with an 89% average), and reveal a strong heterogeneity at the bead scale. Density heterogeneity also seems significant; the lower estimated densities are 10 kg/m^3 whereas the maximum values reach 200 kg/m^3. However, even if this high variation of porosity (i.e., density) is coherent with the visual observations, it is difficult to consider those results as realistic since the noise associated with grey level measurements generates a significant error on local porosity.

Therefore, the grey levels were not used to determine bead densities with accuracy, but only to estimate relative

bead density variations. In the rest of this paper, the densities are provided only to give an indication of foam density heterogeneity and should not be considered exact or absolute. It is then possible to plot the density distribution in the intact sample (before any dynamic loading) as a function of bead position. Recalling that the sample is cut in the middle of the polypropylene foam plate to avoid any density gradient, we should not observe any relation between the two. If we consider bead position in the unloaded sample only in the vertical direction, the plot shown in Fig. 13a reveals a random distribution. On the contrary, if we consider bead position as distance from the centre axis of the cylindrical sample, depicted in Fig. 13b, then a strong density gradient is seen: the densest beads are located around the edges. The mean radius R_m of a bead is about 1.2 mm whereas the sample radius R_s is only 5 mm, this applies that numerous beads are cut during sample preparation. Two regions can be distinguished on the Fig. 13b: a central zone (radius equal to R_s–R_m) where the density is almost constant and a peripheral zone where beads are denser and cut. This can be explained by the induced radial shear caused by the crown saw during sample cutting.

This difficulty met during the sample preparation is well known by researchers and industrials working on polymeric foams. Microtomographic study on larger structure of metallic foams is not affected by similar density heterogeneity since the metallic foam sample machining causes less structure modification (dense material is obviously more rigid) [16].

Further investigation of the volume strain of the beads will allow evaluation of the effects of this wide density distribution, a structural characteristic of the sample, on local deformation.

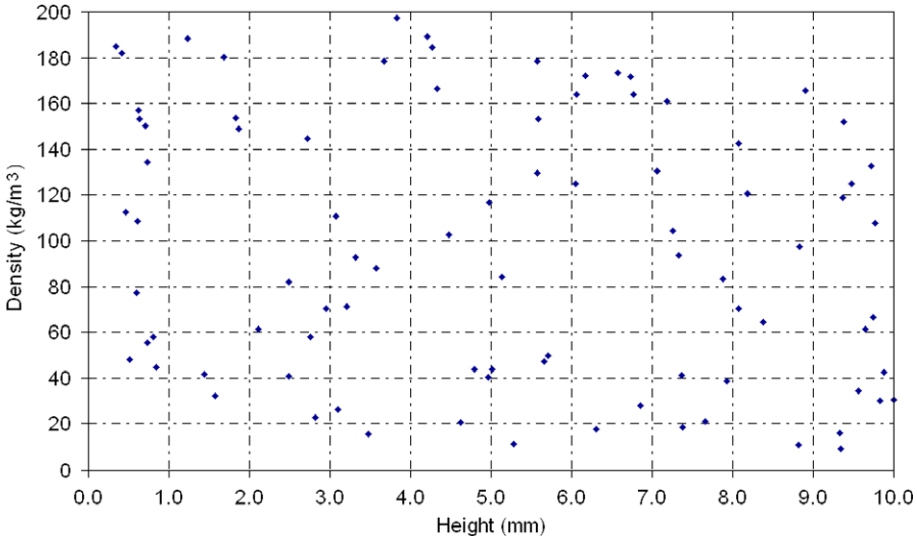

Fig. 13a. Bead density as a function of vertical position in the unloaded sample.

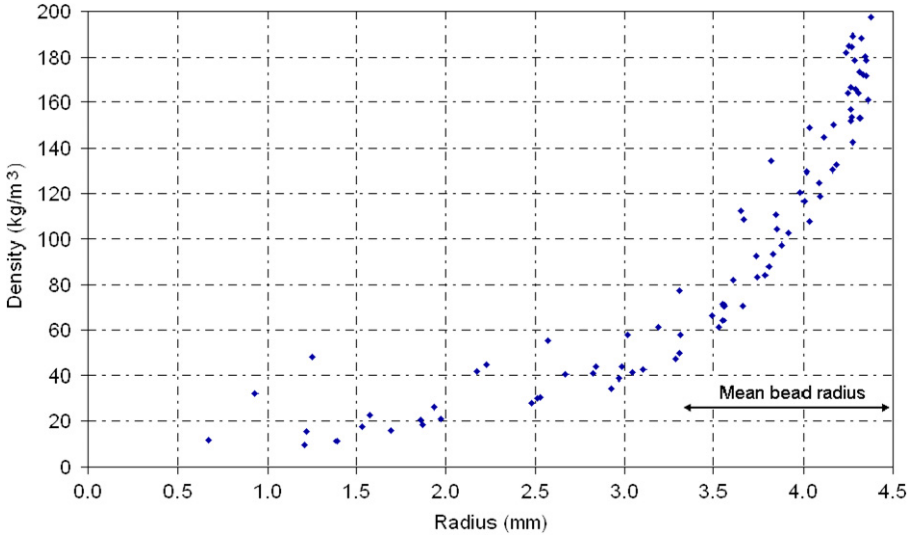

Fig. 13b. Bead density as a function of its radial position in the unloaded sample. The mean bead radius is calculated from the average RBV value.

4.2. Volume strain

The volume strain has been calculated Eq. (5) for each RBV at different loading stages: before the impact, after the first impact when the sample is maintained compressed (point A Fig. 3), after the unloading of the first impact (point A′ Fig. 3), etc. In compressed state, the volume strain corresponds to elastic and plastic volume strain ($\varepsilon^{el}_{i,j}$ and $\varepsilon^{pl}_{i,j}$, respectively), in the unloaded state, the volume strain is equal to the plastic volume strain $\varepsilon^{pl}_{i,j}$. Consequently, $\varepsilon^{el}_{i,j}$ and $\varepsilon^{pl}_{i,j}$ can be determined from the following equations:

$$\begin{aligned} \varepsilon^{pl}_{i,j} &= \varepsilon^{vol}_{i,j,u} \\ \varepsilon^{el}_{i,j} &= \varepsilon^{vol}_{i,j,c} - \varepsilon^{vol}_{i,j,u} \end{aligned} \tag{6}$$

These results show what influences localization of foam strain.

4.2.1. Volume strain vs bead size

The volume strain of the beads has been evaluated at each step of the dynamic loading as a function of their size. Fig. 14 shows the distribution of the volume strain vs the RBV values after the four first impacts when the sample is maintained compressed (points A, B, C and D in Fig. 3). For each step, $\varepsilon^{vol}_{i,j,c}$ distribution is strongly dispersed. However, there is a slight trend that the bigger beads seem to be more deformed than the smaller ones. This trend is more visible after the second impact. In fact, the influence of the bead size is difficult to highlight. The existence of a correlation between bead size and density can be presumed from the moulding process: beads of nearly constant mass are injected in the mould and during expansion, those that are able to occupy a larger volume have a lower density. Therefore, the influence of bead size can be confirmed by analysing the effect of bead density on volume strain.

4.2.2. Volume strain vs bead density

The variation of the volume strain has been established as a function of bead density for the four impacts when the sample is still compressed (Fig. 15a) and after unloading (Fig. 15b). The two configurations lead to the same remarks. For the first impact, a trend in the relation between the density and $\varepsilon^{vol}_{i,j,\alpha}$ can be detected despite a strong scattering. On these figures, fitting curves were plotted to point out these trends, but as indicated by the low value of correlation factor (R^2), they did not allow to quantify an average relation volume strain vs density for each step of the impact. Ignoring this low correlation factor could induce wrong conclusions; volume strain quantification must be restricted to individual bead analysis. The large range of bead volume strain reveals the strong heterogeneity of the deformation field, in particular when the sample is maintained compressed. Stress can be redistributed in the complete sample during the unloading stage inducing a more homogenous strain field and a lower volume strain scattering.

For the most part, the lower the density, the greater the bead volume change. The effect of density is confirmed by the following loading stages, when the macroscopic strain imposed on the sample reaches high values. Lower density beads are significantly compressed whereas the denser ones more rigid and resistant are less deformed.

To conclude on the influence of the foam morphology on its mesoscopic volume strain, we have underlined a significant correlation between bead volume change and density (and size by duality). The previous remarks appear to be evident, as many studies have already shown the influence of the foam density on its macroscopic behavior: typically, denser foam has a higher mechanical response. However, to our knowledge, it is the first time that under dynamic loading and on a multi-scale polymeric foam, the influence of local density on bead deformation is shown

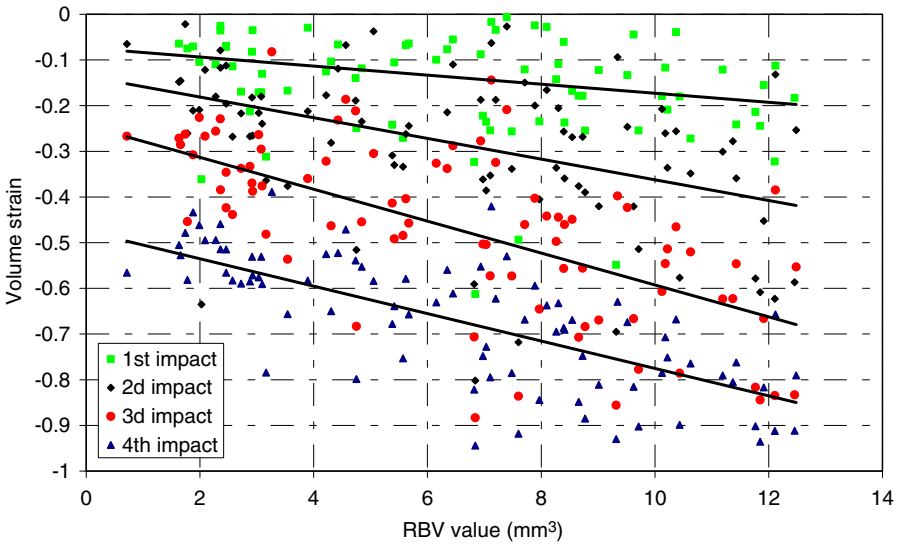

Fig. 14. RBV values as a function of volume strains, plotted for each bead and at each impact stage.

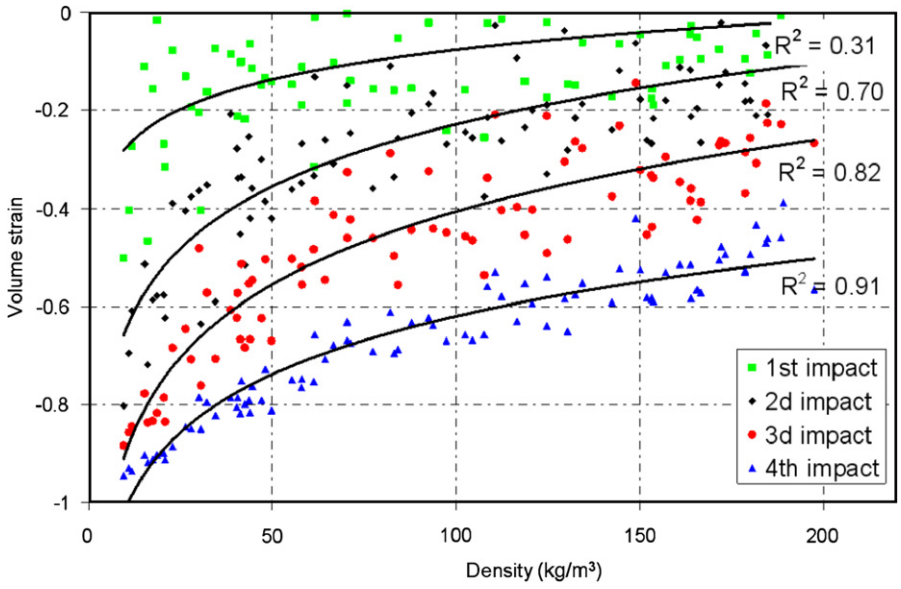

Fig. 15a. Bead density as a function of RBV variation after each impact when the sample is maintained compressed.

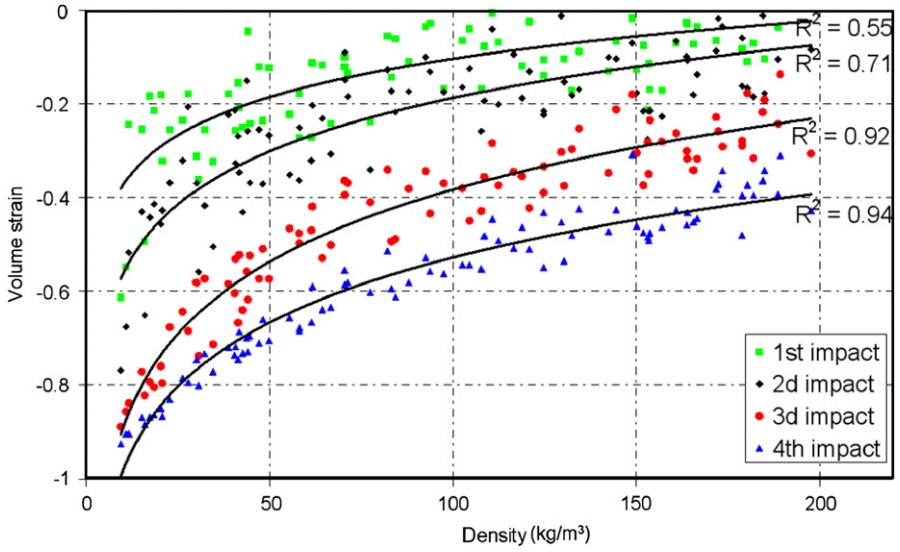

Fig. 15b. Bead density as a function of RBV variation after each unloading stage.

at the mesoscopic scale. To complete this study and qualify the strain-density correlation, localization of foam strain has been analysed.

4.2.3. Volume strain vs bead position

For each impact, bead volume strains were plotted vs barycentre positions; the objective being to detect any localization of the strain at the scale of the sample. The coordinates of the bead barycentres are defined in a cylindrical system (r, θ, Z) since the sample is axi-symetric. Given that θ has no influence (this hypothesis has been checked), the beads (identified by a number, Fig. 16) are classified according to the vertical and radial positions, Z and r respectively, of their barycentres. For the sake of clarity, the results are separated, firstly for Z, in five 2 mm high horizontal slices of the sample, and secondly for r, in two cylindrical regions of identical volume: a central cylinder (3.53 mm in diameter) and its outlying tube. Each bead is then assigned a horizontal slice and a cylindrical region. For each defined portion of the sample, the average bead volume strain is calculated, and this process is repeated for each impact.

4.2.3.1. Volume strain vs vertical position. The dependence of the strain $\varepsilon_{i,j,\alpha}^{\mathrm{vol}}$ on the slice number is illustrated in Fig. 17. Each diagram presents the average volume strain of the RBVs belonging to the five vertical slices for each impact with the sample still compressed or unloaded. Slice one corresponds to the bottom of the sample and slice five

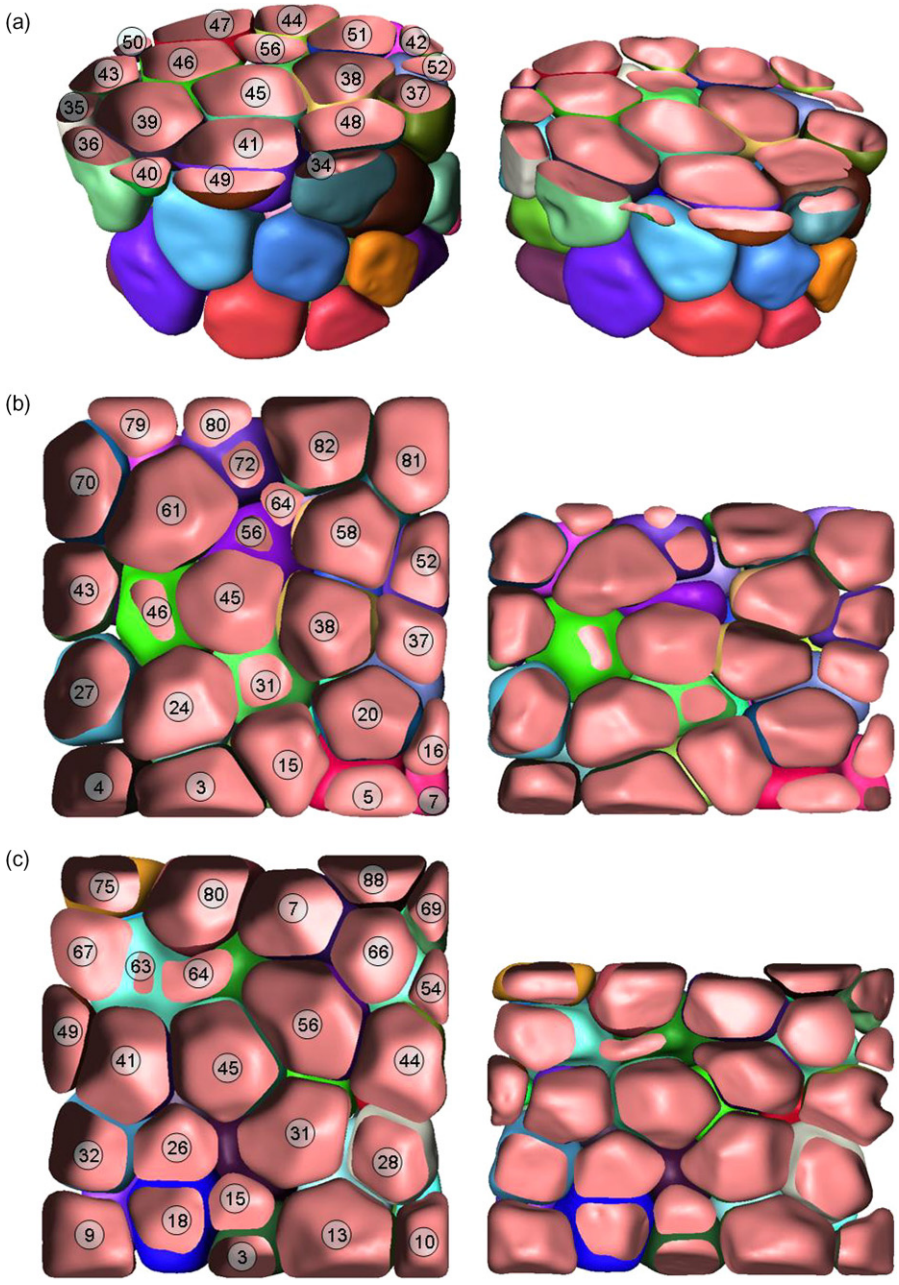

Fig. 16. Slices in different directions (a: XY or axial, b: XZ or coronal, c: YZ or sagittal) of the RBVs for two stages: before impact (left), and after the second impact (right). Beads are all identified by a number.

to the top of the sample, in contact with the compression punch.

For the first impact, the distribution of volume strain according to the slice number is clearly established: the slices closer to the compression surfaces of punch and die are more deformed than average (the global strain is 10%) whereas the centre slice is only lightly deformed (5%). This is verified in both the compressed and unloaded states. Moreover, the most deformed slice (number 5) is the one against the punch that inflicts the loading. Visual inspection of bead and cell wall deformation corroborates this analysis [17]. Several factors could explain this behavior, and they can be associated with the type of compression and with the morphology of the structure. Firstly, concerning the compression procedure, the contact of the sample with the rigid surfaces of the punch and die can generate a greater deformation for border beads, especially during a dynamic loading. There is not necessarily homogeneous stress field in the sample at the beginning of the test. The punch generates a shock wave at the upper surface of the sample that induces a stress localization in its upper part (slice 5) and then higher strain values (this phenomenon has been already experimentally shown, in the case of dynamic loading of cellular materials, measuring

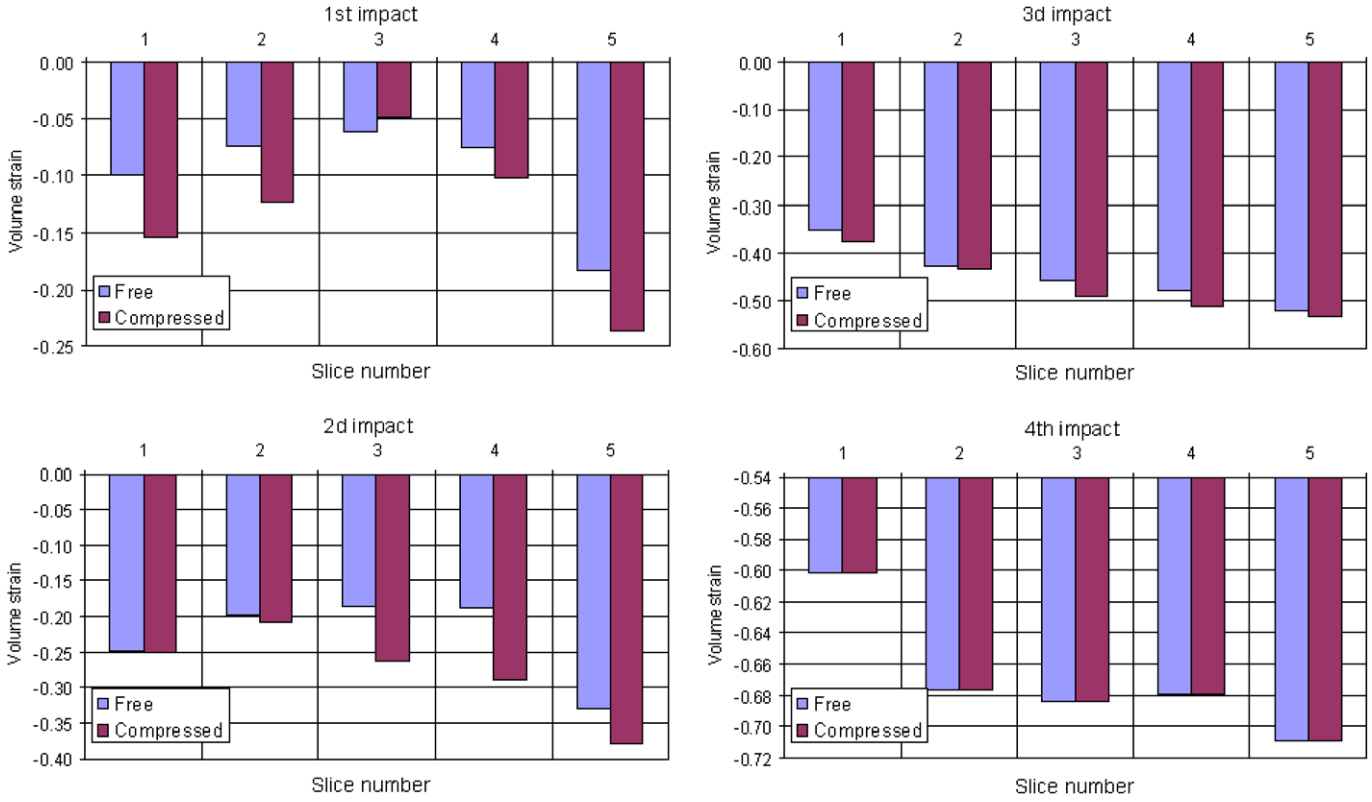

Fig. 17. Average volume strain for the five horizontal slices as a function of impact steps.

difference of forces on both sides of the sample during a test with Hopkinson Bar [24]). Consequently, at the beginning of the test, the compression force is concentrated on slice 5 generating higher deformation. Secondly, and this concerns the preparation of the sample, the outer beads in contact with the punch and die have been cut and are thus weakened by the loss of part of their walls. The morphology of the foam structure is different in these two zones and can contribute to the modification of the local behavior.

For the second impact, the observed phenomena are similar. The global deformation imposed on the sample is 30%. In the compressed state, the higher slices are the most deformed: the volume strain of slice 5 reaches 38% whereas slice 2 is just deformed by 20%. Again, the beads in contact with the rigid surfaces of the die and punch are particularly deformed. It is also interesting to compare the volume strains ε^{el} and ε^{pl}. The volume strain ε^{pl} is nearly constant (20%) for slices 2, 3 and 4 after the second impact, but in its compressed state, a strong difference on ε^{vol} can be noted, meaning that the elastic strain ε^{el} is still significant for slices 3 and 4. On the contrary, ε^{el} is particularly weak for slices 1 and 5.

For the last impacts (deformations of 50% and 70%), ε^{vol} is more homogeneous and a slope is observed in the variation of the volume strain according to the slice number. At these levels of compression, the cellular material deformation becomes mainly plastic (the sample is in the densification phase after the 4th impact) and the elastic response is very low.

The response of the polypropylene foam measured during the impact corresponds to a typical behavior for a cellular material; an elastic response followed by a plastic plateau and finally a densification [6,25]. The heterogeneity of ε^{vol} put into evidence in this work and its variation depends on the combination of the effect of the dynamic loading (certainly due to a propagation of a shock wave during the impact) and the effect of the foam microstructure (some bead walls have been removed during the sample preparation).

4.2.3.2. Volume strain vs radial position. Finally, bead volume strain is compared to radial position in Table 1. Values of ε^{vol} in the periphery are lower than those in the central region after each impact and for compressed or unloaded states. This variation in strain according to radial position can be explained by density and structure effects. There is a dependency of the density on the radial position; the denser peripheral beads constitute a rigid shell for the core of the sample. During the compression, the volume variation of this external shell skin is low, and its thickness increases while its height decreases. The increase in thickness implies a radial stress imposed on the central beads; The loading is in fact a combination of a uniaxial compression and a radial pressure. Therefore, this particular heterogeneous microstructure in terms of bead density generates a stress field between beads that is more complex than the uniaxial compression imposed by the punch. This

Table 1
Volume strain mean as a function of the radial position (internal or external) of beads for each impact

	1st impact		2nd impact		3rd impact		4th impact	
	Compressed	Unloaded	Compressed	Unloaded	Compressed	Unloaded	Compressed	Unloaded
Internal zone	−0.24	−0.17	−0.43	−0.38	−0.64	−0.63	−0.82	−0.76
External zone	−0.07	−0.06	−0.18	−0.14	−0.35	−0.32	−0.57	−0.47

Table 2
Volume strain for four beads calculated for the second, third and fourth impact (in the compressed and unloaded states)

Bead number	Density	2nd impact		3rd impact		4th impact	
		Unloaded vol. strain	Compressed vol. strain	Unloaded vol. strain	Compressed vol. strain	Unloaded vol. strain	Compressed vol. strain
45	84.2	−0.22	−0.26	−0.49	−0.56	−0.61	−0.69
61	93.8	−0.13	−0.17	−0.43	−0.44	−0.56	−0.64
31	178.7	−0.16	−0.18	−0.29	−0.37	−0.48	−0.53
41	178.8	−0.06	−0.15	−0.28	−0.29	−0.40	−0.53

hypothesis is confirmed when observing the shape of the deformed beads [17].

4.2.4. Volume strain of individual beads

To confirm that density is not the only parameter that acts on sample deformation, volume strain was examined for all the individual beads. As the objective is not to deduce an average behavior but to highlight the complexity of the local response, we only present the results for four representative beads. They have been selected in the centre of the sample since deformation in this area seems more homogeneous. Fig. 16 allows visualising the positions and shapes of these beads. Table 2 indicates the bead number and density, and gives the volume strains calculated for the three last impacts (the results for the first impact are not significant). When comparing the volume strains calculated for beads 31 and 41 (of equal density) after the second impact, one observes obvious differences. Similarly, volume strain of bead 45 is higher than the one of bead 61 whereas their densities are equivalent. On the other hand, between beads 61 and 31, deformation is similar but bead 31 has a higher density.

Consequently, it is clear that if bead density has an influence on local deformation, the real morphology of the mesostructure (size and shape of the beads, their spatial localization, thickness of the bead walls [17], etc.) must also be taken into account to improve constitutive model of this multi-scale material.

5. General conclusion and perspectives

This article presents the last results of a work on the analysis of the localization of foam strain at mesoscopic scale (bead scale). To reach these results and describe the mesoscopic strain distribution of a polypropylene foam sample under dynamic loading, a new approach has been developed in combining original impact device, micro tomography techniques and specific image algorithms in more demanding conditions (multi-scale material and dynamic loading) than in already published works. Firstly, dynamic compression interrupted tests were carried out on polypropylene foam samples and microtomographic acquisitions made after each impact. A customized image processing method has been developed and applied to extract a representative volume of each bead from the complex microstructure of the multi-scale foam. The change of the meshed deformable surfaces obtained at the different steps of the dynamic compression allows determination of the porosity variation of beads and their volume strain.

The distribution of the bead density has been examined as a function of its radial and axial location. No axial correlation appeared whether a strong radial one can be detected. That has been interpreted as a consequence of the sample preparation. The existence of this heterogeneous density distribution might be problematic for macroscopic behavior identification but is less important in our objective since next step is the modeling of the real sample mesostructure (bead scale).

The volume strain distribution was analysed as a function of bead size, density and location for all the steps of the impact at the compressed and unloaded states. A slight influence of bead size has been shown; the larger beads are generally more deformed. However, the main correlation appeared with density; the lower the density, the greater the bead volume change. This correlation is valid for all the loading stages. Finally, the axial and radial location of the beads affects their volume strain in a complex way that is globally explained by a combination of dynamic loading and foam microstructure effects.

Those results demonstrate that bead density has an influence on local deformation but the real morphology of the mesostructure (size and shape of the beads, their spatial localization, thickness of the bead walls [17], etc) has to be taken into account to explain the detailed mesoscopic behavior. The analysis of data concerning specific beads reinforced the conclusion: bead density and volume change

are not completely correlated. A companion study using our micro tomograms and 3D Digital Image Correlation techniques [23] confirms our measurements of the mean volume change on a bead (labelled 61) and, furthermore, highlights, almost at the cell scale, the heterogeneity of strain inside this bead.

From the results presented and their analysis, the behavior of this polypropylene foam structure is better understood at mesoscopic scale. The next step of this work is the modeling of the foam morphology (bead and cell structures) taking into account the observed phenomena. A multi-scale model will be developed representing the dense bead walls (mesoscopic scale) by a surface mesh (with properties of dense polypropylene) and the porous interior of the beads by a volume model based on Discrete Elements.

Acknowledgements

We acknowledge the *European Synchrotron Radiation Facility* for provision of synchrotron radiation facilities.

We would like to thank the two anonymous reviewers that significantly helped in improving the final version of the paper.

References

[1] Di Landro L, Sala G, Olivieri D. Deformation mechanisms and energy absorption of polystyrene foams for protective helmets. Polym Test 2002;21(2):217–28.

[2] Song B, Chen WW, Dou S, Winfree NA, Kang JH. Strain-rate effects on elastic and early cell-collapse responses of a polystyrene foam. Int J Impact Eng 2005;31(5):509–521x.

[3] Avalle M, Belingardi G, Montanini R. Characterization of polymeric structural foams under compressive impact loading by means of energy-absorption diagram. Int J Impact Eng 2001;25(5):455–72.

[4] Zhang J, Kikuchi N, Li V, Yee AF, Nusholtz GS. Constitutive modeling of polymeric foam material subjected to dynamic crash loading. Int J Impact Eng 1998;21(5):369–86.

[5] Zhang J, Lin Z, Wong A, Kikuchi N, Li VC, Yee AF, et al. Constitutive modeling and material characterization of polymeric foams. Int J Eng Mater Technol 1997;119(3):284–91.

[6] Gibson LJ, Ashby F. Cellular solids. Structures and properties. Solid State Science Series. Cambridge; 1997.

[7] Gibson LJ, Zhang J, Shercliff TL. Failure surface for cellular materials under multi-axial loads I.Modeling. Int J Mech Sci 1989;31(9):635–63.

[8] Chen C, Deshpande VS, Fleck NA. A constitutive model for a transversely isotropic compressible solid: user manual for a UMAT in ABAQUS. Cambridge University Engineering Department; Internal Report CUED/C-MICROMECH/TR.93, 2003.

[9] Hallquist JO. LS-DYNA3D theoretical manual. LSTC Report 1018; 1994.

[10] Viot P, Beani F, Lataillade J-L. Polymeric Foam behavior under dynamic compressive loading. Int J Mater Sci 2005;40(22):5829–37. doi:10.1007/s10853-005-4998-5.

[11] Viot P, Vacher P. Identification of foam behavior under dynamic loading by the use of particle imaging techniques. Revue Matériaux et Techniques, Hors série: 39–43, December 2004. ISSN 0032-6895.

[12] Baruchel J, Buffière JY, Maire E, Merle P, Peix G. X-ray tomography in material science. Paris: Hermes Sciences Publishers; 2000.

[13] Brunkea O, Odenbach S, Beckmann F. Quantitative methods for the analysis of synchrotron-μ CT datasets of metallic foams. Eur Phys J Appl Phys 2005;29:73–81.

[14] Elmoutaouakkil A, Fuchs G, Péres R, Peyrin F. Three-dimensional quantitative analysis of polymer foams from synchrotron radiation X-ray microtomography. J Phys D: Appl Phys 2003;36:A37–43.

[15] Knackstedt MA, Arns CH, Saadatfar M, Senden TJ, Limaye A, Sakellariou A, et al. Elastic and transport properties of cellular solids derived from 3D tomographic images. Proc Roy Soc A 2006;462: 2833–2862.

[16] McDonald SA, Mummery PM, Johnson G, Withers PJ. Characterization of the three-dimensional structure of a metallic foam during compressive deformation. J Microsc 2006;223(2):150–8.

[17] Viot P, Bernard D, Plougonven E. Polymeric foam deformation under dynamic loading by the use of the microtomographic technique. J Mater Sci 2007;42(17). doi:10.1007/s10853-006-1422-8.

[18] Cloetens P, Barrett R, Baruchel J, Guigay J-P, Schlenker M. Phase objects in synchrotron radiation hard X-ray imaging. J Phys D: Appl Phys 1996;29(1):133–46.

[19] Kong TY, Rosenfeld A. Digital topology: introduction and survey. Comput Vision Graph 1989;48(3):357–93.

[20] Heijmans HJ. Mathematical morphology: a modern approach in image processing based on algebra and geometry. SIAM Rev 1995;37(1):1–36.

[21] Delingette H. Modélisation, déformation et reconnaissance d'objets tridimensionnels à l'aide de maillages simplexes. Ph.D. thesis, Ecole centrale de Paris; 1994.

[22] Montagnat J, Delingette H, Scapel N, Ayache N. Representation, shape topology and evolution of deformable surfaces. Application to 3D medical image segmentation; Research Report No. 3954, INRIA; 2000.

[23] Roux S, Hild F, Viot P, Bernard D. Three-dimensional image correlation from X-ray computed tomography of solid foam Composites A [in press]. Available online 4 December 2007.

[24] Zhao H. Testing of polymeric foams at high and medium strain rates. Polym Test 1997;16(5):507–16.

[25] Mills N. Polymer foams handbook. Butterworth-Heinemann; 2007, ISBN10: 0-7506-8069-5.